

Interfacial Dipole Engineering via Boronic Acid-Based Self-Assembled Monolayers in Inverted Tin–Lead Perovskite Solar Cells with Ideal Band Gap

Safalmani Pradhan,* Huān Bi, Gaurav Kapil, Aruto Akatsuka, Ajay Kumar Baranwal, Dandan Wang, Dong Liu, Suraya Shaban, Takeshi Kitamura, Shahrir Razey Sahamir, Yasuhiro Fujiwara, Jiaqi Liu,* Hiroshi Segawa, Hiroyuki Yoshida, Qing Shen,* and Shuzi Hayase*



Cite This: *ACS Energy Lett.* 2025, 10, 4983–4994



Read Online

ACCESS |



Metrics & More

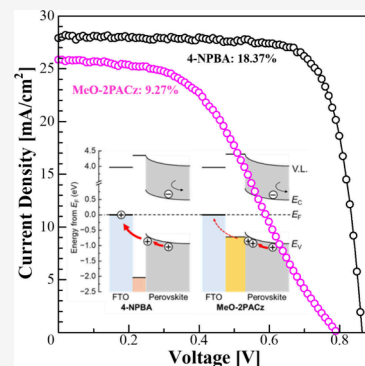


Article Recommendations



Supporting Information

ABSTRACT: According to the detailed balance limit for a single-junction solar cell, perovskites with a 1.4 eV band gap can theoretically achieve power conversion efficiencies (PCEs) above 33%, but their progress is limited by the hygroscopic nature of PEDOT:PSS and incompatibility with self-assembled monolayers (SAMs) like MeO-2PACz. Using boronic acid (BA)-based SAMs, especially 4-nitrophenyl boronic acid (4-NPBA), the PCE was greatly improved (18.37%). This is attributed to the large molecular dipole moments of the BA-based SAMs significantly increasing the work function (WF) of the FTO, inducing stronger band bending in the perovskite layer. This band bending, whose magnitude is proportional to the difference in the WF between the SAM and the perovskite, facilitated more efficient hole collection. In comparison, MeO-2PACz-based devices yielded only 9.27% and showed an S-shaped current–voltage (I – V) curve, mainly due to the formation of an interfacial energy barrier. Furthermore, the superior performance of the BA-based SAMs even after possessing an interfacial energy barrier can be explained by enhanced hole collection via (i) tunneling aided by short molecular length of BA-based SAMs as calculated by density functional theory (DFT), or (ii) direct hole transfer from perovskite to FTO through the uncovered FTO regions due to lower surface coverage as evidenced by absorption density estimation in X-ray photoelectron spectroscopy (XPS). These findings were further supported by transient absorption (TA) as well as transient photocurrent decay (TPC) analyses, which revealed markedly higher hole extraction rate ($3.73 \times 10^{-3} \text{ ps}^{-1}$) and lower charge transport time ($1.18 \mu\text{s}$) when 4-NPBA was used as a SAM layer.



Since their discovery in 2009, perovskite solar cells (PSCs) have made notable advances as their power conversion efficiencies (PCEs) have increased from 3.8% to over 27.3% within a short span of 15 years.^{1–4} PSCs have advanced rapidly as a result of their extraordinary optoelectronic properties, including tunable direct band gaps, long carrier diffusion lengths exceeding $1 \mu\text{m}$, remarkable defect tolerance, low exciton binding energies, and a high optical absorption coefficient ($\sim 10^5 \text{ cm}^{-1}$).⁵ The most significant advantage of PSCs is their low cost and solution processable fabrication technique.^{6,7} However, the solution-based fabrication of perovskite films can generate surface and grain boundary defects, which act as sites for nonradiative recombination. These defects contribute to energy losses and reduce both the open-circuit voltage (V_{oc}) and fill factor (FF).^{8,9} Moreover, the misalignment of energy levels at the

interface enhances carrier recombination losses, thus limiting the overall performance. Therefore, it is crucial to maintain proper interfacial energy level alignment for preventing these energy losses and improving the photovoltaic performance of PSCs.^{10,11} Interfacial engineering strategies using various interfacial materials and passivation techniques has been widely adopted to minimize the energy losses and enhance the PCE of the devices.^{12,13} Poly(3,4-ethylenedioxythiophene):poly(styrenesulfonate) (PE-

Received: June 21, 2025

Revised: August 17, 2025

Accepted: September 15, 2025

DOT:PSS)-based hole transport layers (HTLs), although widely used, suffer from hygroscopic and acidic nature, thereby leading to perovskite degradation, adversely impacting the operational stability of PSCs.^{14–16} In this context, self-assembled monolayers (SAMs) are widely used for improving the charge transport and mitigating interfacial recombination.^{17,18} Upon adsorption on the substrate, SAMs create strong interfacial dipoles that can effectively modify the substrates' work function (WF), resulting in interfacial band bending. The resulting band alignment enhances charge selectivity of the substrate, facilitating charge extraction and suppressing recombination.^{19,20} Phosphonic acid-based SAMs, namely, [2-(3,6-dimethoxy-9H-carbazol-9-yl)ethyl]phosphonic acid (MeO-2PACz) and [2-(9H-carbazol-9-yl)ethyl]phosphonic acid (2PACz), have achieved high PCEs by minimizing charge recombination and providing good energy level alignment in lead (Pb) halide perovskites as well as in narrow band gap mixed tin–lead (Sn–Pb) perovskites.^{21–24} Further, the PCEs of single-junction PSCs were enhanced by adopting a co-SAM strategy^{24–26} and self-assembled bilayer strategy.²⁷ However, the insulating property of the alkyl linker between the phosphonic acid and the carbazole moiety as well as their low stability under high-energy ultraviolet (UV) photons limits the performance of these SAMs.^{28,29} Furthermore, the PCE of PSCs incorporating SAMs varies markedly with the perovskite composition and the specific device architecture employed. For example, tin halide perovskites have reached a maximum PCE of 9.4% when employing SAMs as HTL, whereas a significantly higher PCE of 17.13% has been achieved when employing PEDOT:PSS, highlighting the impact of interface engineering on device performance.^{30,31} Another such composition exhibiting incompatibility with traditional SAMs like MeO-2PACz and 2PACz is the ideal band gap (1.4 eV) mixed Sn–Pb perovskite. This perovskite composition has gained significant attention due to its ability to achieve an optimal balance between voltage and current generation, theoretically enabling the maximum PCE (~33%) as predicted by the Shockley–Queisser (SQ) limit for single-junction solar cells under standard AM 1.5G illumination.^{32,33} However, their compatibility with MeO-2PACz has been constrained by energy level misalignment that creates an interfacial energy barrier unfavorable for hole collection. In addition, poor film formation resulting from surface wettability issues further limits device performance.^{34–36} Although recent research has effectively addressed the concerns of surface wettability, the problem of suboptimal energy level matching prevails across a wide range of perovskite compositions, thereby resulting in substantial performance losses.^{37,38} Current strategies to mitigate these issues include the incorporation of organic molecules with optimal dipole moments for efficient interfacial engineering.^{17,39,40} These organic molecules possess a dipole moment arising from the spatial separation of positive and negative charges, which modifies the substrate's WF, thereby significantly influencing the charge carrier transport at the interface.⁴¹ For instance, incorporating donor– π –acceptor (D– π –A) dipoles at the perovskite/electron transport layer (ETL) interface has been shown to increase the built-in electric field and lower the WF.⁴² Similarly, the dual strategy of surface passivation and construction of interfacial dipoles via an azaindole derivative led to reduction in surface defects, excellent energy level alignment, and reduced nonradiative recombination.⁴³ However, the orientation and magnitude of surface dipoles depend

on the specific interactions between molecules and the surface, enabling them to either raise or lower the WF. Therefore, judiciously engineered dipoles are essential for optimizing energy level alignment and facilitating efficient directional charge extraction and transport.^{44,45} However, it is important to note that the effective WF modulation also depends on packing density, molecular as well as dipole orientation.^{46–48}

This study reports the strategic implementation of boronic acid (BA)-based SAMs with suitable para-substituted functional groups, namely, 4-nitrophenyl boronic acid (4-NPBA), 4-cyanophenyl boronic acid (4-CPBA), 4-trifluoromethylphenyl boronic acid (4-TFPBA), and 4-fluorophenyl boronic acid (4-FPBA), to tailor their net dipole moments and modulate the WF of FTO. MeO-2PACz possessing the lowest net dipole moment among the five SAMs was used as a reference. The main purpose of using SAMs with varying dipole moments is to modify the WF of FTO through their molecular orientation induced by their permanent dipole moments. Furthermore, the chemical interactions at the SAM/perovskite interface due to the presence of different end functional groups influence the crystallinity and morphology of perovskite films.^{43,49,50} Gaussian calculations show that the gas-phase dipole moments of these SAMs reduce in the order of 4-NPBA (8.21 D) > 4-CPBA (7.67 D) > 4-TFPBA (6.05 D) > 4-FPBA (4.57 D) > MeO-2PACz (1.27 D). In the case of BA-based SAMs, this dipole is oriented from the end functional group toward the anchoring group (i.e., away from the perovskite). This particular orientation of dipole moment where the negative end of the dipole is toward the perovskite is expected to increase the WF difference between the SAM-modified FTO and the perovskite, resulting in a favorable band bending at the SAM/perovskite interface, thereby improving hole extraction.^{51,52} The fabrication of PSCs using perovskite precursor $\text{Cs}_{0.15}\text{FA}_{0.8}\text{Rb}_{0.05}\text{Sn}_{0.25}\text{Pb}_{0.75}\text{I}_{2.5}\text{Br}_{0.5}$ (referred to as “perovskite” hereafter) on 4-NPBA-modified FTO substrate led to an achievement of a PCE of 18.37% with increased V_{oc} of 0.86 V, short-circuit current density (J_{sc}) of 27.88 mA/cm^2 , and FF of 0.76, owing to its large dipole moment and enhanced WF. For the boronic acid (BA)-based SAMs, the magnitude of band bending at the SAM/perovskite interface and their photovoltaic performance correlated well with their respective dipole moments, with higher-dipole SAMs producing stronger band bending and thus better PCE. Contrary to this trend, MeO-2PACz, despite having a lower molecular dipole moment, produced the largest WF and strongest band bending, mainly due to better molecular orientation, higher packing density, and stronger bonding with the substrate. However, despite these advantages, its PCE was the lowest (to be discussed later). Although, BA-based molecules have been used in organic solar cells (OSCs)⁵³ as SAMs and also in PEDOT:PSS incorporated Pb-based PSCs (1.5 eV) to modulate the WF of indium-doped tin oxide (ITO),⁵⁴ in this work we employ BA-based SAMs as an alternative to PEDOT:PSS to tune the WF of FTO in ideal band gap Sn–Pb PSCs. The ideal band gap PSCs (1.3–1.4 eV) incorporating metal organic framework (MOF)-based hole-transporting materials (HTMs)⁵⁵ as well as bulky organic HTMs⁵⁶ have been reported in the literature. In addition to this, PEDOT:PSS-free ideal band gap Sn–Pb PSCs incorporating poly[bis(4-phenyl)(2,4,6-trimethylphenyl)amine (PTAA)⁵⁷ and nickel oxide (NiO_x)⁵⁸ have also been reported in the literature. However, to the best of our knowledge, this is the first report on ideal band gap Sn–Pb PSCs incorporating ultrathin organic SAMs.

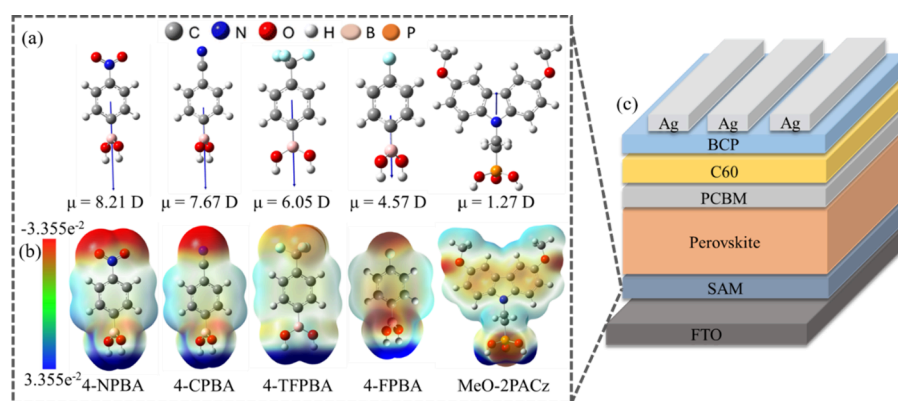


Figure 1. (a) Gaussian optimized molecular structures of different SAMs; (b) electrostatic potential (ESP) maps of different SAMs; (c) schematics showing the device architecture used in this study.

The chemical structure of the SAMs, their density functional theory (DFT) optimized molecular structures, as well as their electrostatic potential (ESP) mapping estimated using Gaussian are shown in Figures S1 and 1a,b, respectively. Figure S2a,b shows the third-quarter and side views of the DFT-optimized molecular structure of MeO-2PACz along with its ESP map. Figure 1c shows the schematics of the device architecture used in this study. The ESP mapping reveals that the strongly electron-withdrawing nature of the $-\text{NO}_2$ functional group significantly enhances the electron cloud density at the SAM/perovskite interface. This leads to a substantial net molecular dipole, which facilitates effective trap passivation and favorable band energy alignment.^{59,60} The strength of this effect follows the order 4-NPBA > 4-CPBA > 4-TFPBA > 4-FPBA \gg MeO-2PACz, correlating with the electron-withdrawing ability of each functional group. X-ray photoelectron spectroscopy (XPS) analysis confirmed the adsorption of SAMs on the FTO surface, as illustrated in Figure S3. The binding energies in the XPS spectra were calibrated by setting the C 1s peak (Figure S3a) to 284 eV for accurate energy referencing. The presence of fluorine (F) in 4-TFPBA and 4FPBA-modified FTO substrates was confirmed by the appearance of an enhanced F 1s peak in the XPS spectrum of SAM-coated FTO, indicating successful incorporation or surface enrichment of fluorine upon SAM deposition (Figure S3b). The detection of N 1s signals in the XPS spectra (Figure S3c) of FTO substrates modified with 4-NPBA, 4-CPBA, and MeO-2PACz confirmed their successful adsorption. Further, the reduction in the intensity of the Sn 3d_{5/2} peak (due to FTO) in the SAM-modified FTO relative to bare FTO as well as the change in its binding energy confirms the adsorption of SAMs on FTO (Figure S 3d). In addition to this, the adsorption of these SAMs on the FTO surface is proven by the disappearance or significant reduction in the intensity of peaks associated with Sn–O vibrational modes of FTO in the infrared (IR) spectra (Figure S4).

As discussed earlier, the PSC fabricated on FTO substrates modified by BA-based SAMs exhibited a better PCE in comparison to the PSCs fabricated on the MeO-2PACz-modified FTO substrate. With a PCE of only 9.27%, MeO-2PACz-based PSCs exhibited an S-shaped current–voltage (I – V) curve. To rationalize this observation, the influence of different SAMs on the perovskite crystal structure was investigated by X-ray diffraction (XRD). The observed diffraction peaks (Figure 2a) with characteristic reflections from the (100), (110), (111), (200), (210), (211), (220),

(300), and (222) planes indicate the formation of a three-dimensional perovskite crystal lattice with pseudocubic or tetragonal symmetry.^{61,62} The intensity of the (100) peak at $\sim 14.58^\circ$ (Figure 2b), often used as an indicator of preferential crystal orientation,^{63,64} followed the trend 4-NPBA > 4-CPBA > 4-TFPBA > 4-FPBA > MeO-2PACz, which also correlated with their respective dipole strength. This suggests that the interfacial dipole introduced by BA-based SAMs due to various end functional groups provides favorable surface energy conditions leading to highly oriented crystal growth along the (100) plane. Further, as observed in Figure 2a, the perovskite films also exhibited a preferential orientation along the (110) plane. Furthermore, we analyzed the full width at half maximum (FWHM) of the (100) peak (Figure 2c and Table S1) after XRD peak fitting analysis for evaluating perovskite crystallinity.⁶² The XRD peak fitting analysis showed that the perovskite film deposited on the 4-NPBA-modified FTO substrate exhibited a FWHM of 0.0975° and crystal size of 858.16 Å. These values exhibited by perovskite film deposited on 4-NPBA-modified FTO were best among all the SAMs used, therefore indicating enhanced film crystallinity. The perovskite films deposited on other SAM-modified FTO substrates showed similar FWHM values and crystal sizes, suggesting a comparable crystallinity across those samples. However, the improvement of FWHM and crystal size for the perovskite film deposited on the 4-NPBA-modified FTO substrate is not substantial enough to attribute the improvement of photovoltaic performance solely to it. Furthermore, the calculated d -spacing values were found to be nearly identical, ranging from 6.0676 to 6.0704 Å. This suggests that the incorporation of different SAMs does not significantly affect the lattice parameter of the perovskite structure, indicating that the overall crystal phase remains consistent across the various interface modifications. To further assess film quality, scanning electron microscopy (SEM) was employed to examine the surface morphology of perovskite films deposited on various SAM-modified FTO substrates, as shown in Figures 2d–h. Apart from the perovskite film deposited on the 4-NPBA-modified FTO, which exhibited enlarged grain domains and a more compact morphology (consistent with its relatively narrower FWHM), the perovskite films deposited on other SAM-modified FTO substrates displayed similar surface morphologies with comparable grain sizes. Figure S5 shows the atomic force microscopy (AFM) images where the surface roughness (root-mean-square, RMS) of these perovskite films ranges between 21 nm (FTO/4-

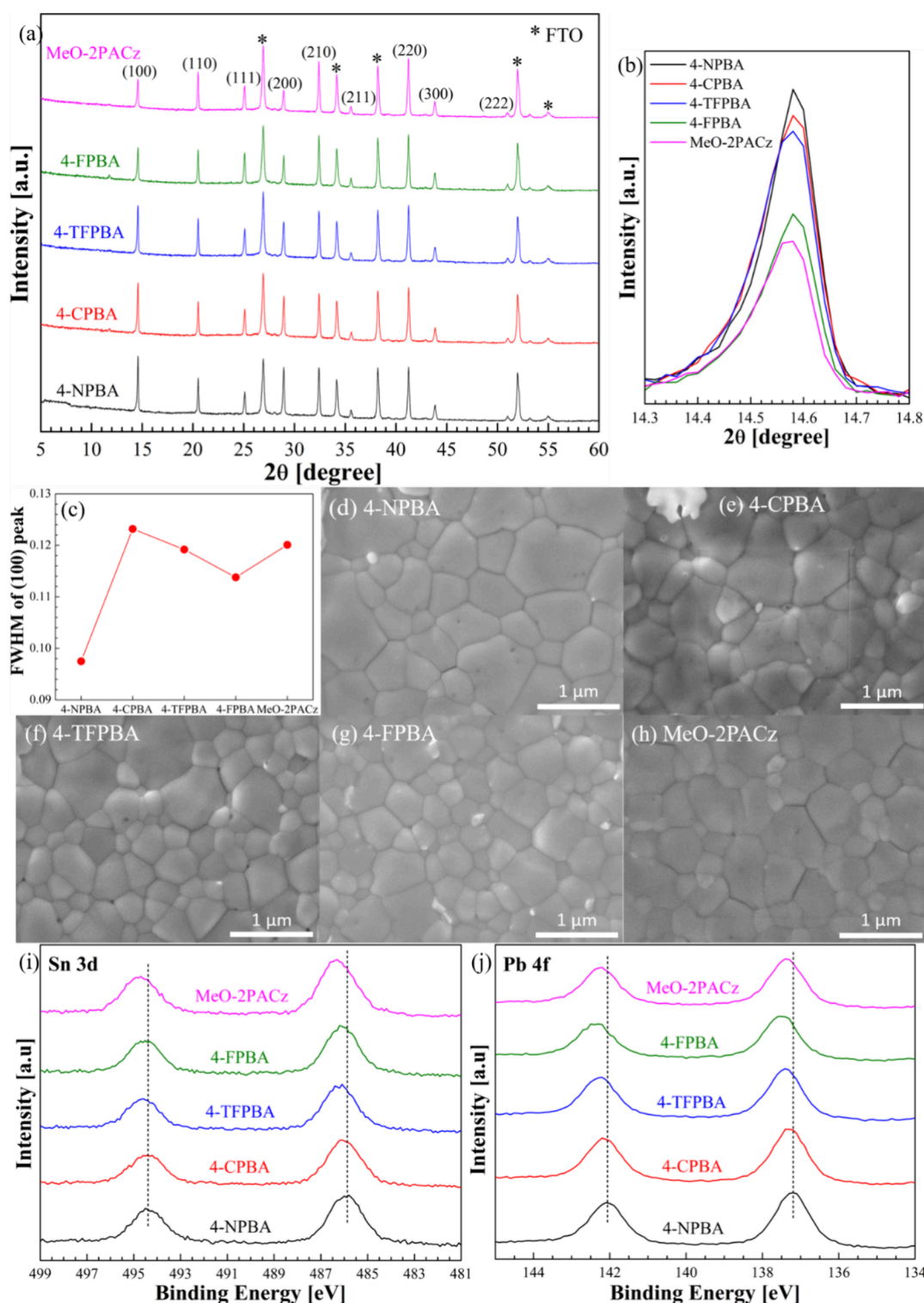


Figure 2. (a) XRD spectra, (b) XRD spectra showing (100) peak intensity, and (c) variation of full width at half maximum (FWHM) for the perovskite films deposited on various SAM-modified FTO substrates. Surface morphology of perovskite films deposited on (d) 4-NPBA; (e) 4-CPBA; (f) 4-TFPBA; (g) 4-FPBA; (h) MeO-2PACz – modified FTO substrates. X-ray photoelectron spectroscopy (XPS) showing (i) Sn 3d and (j) Pb 4f spectra of perovskite films deposited on various SAM-modified FTO substrates.

NPBA/perovskite) and 27.5 nm (FTO/MeO-2PACz/perovskite). These analyses revealed comparable film quality across all SAMs, except for the 4-NPBA case, which showed slightly reduced FWHM for the (100) XRD peak and enlarged grain size partially explaining its superior performance. However, the enhanced PCEs observed for other BA-based SAMs over

MeO-2PACz remain unexplained. Figure 2i,j shows the XPS spectra of Sn 3d and Pb 4f core levels, respectively, for the perovskite films deposited on various SAM-modified FTO substrates. The binding energies were calibrated by setting the C 1s peak shown in Figure S6a to 284 eV for accurate energy referencing. Figure S6b shows the I 3d spectra for the

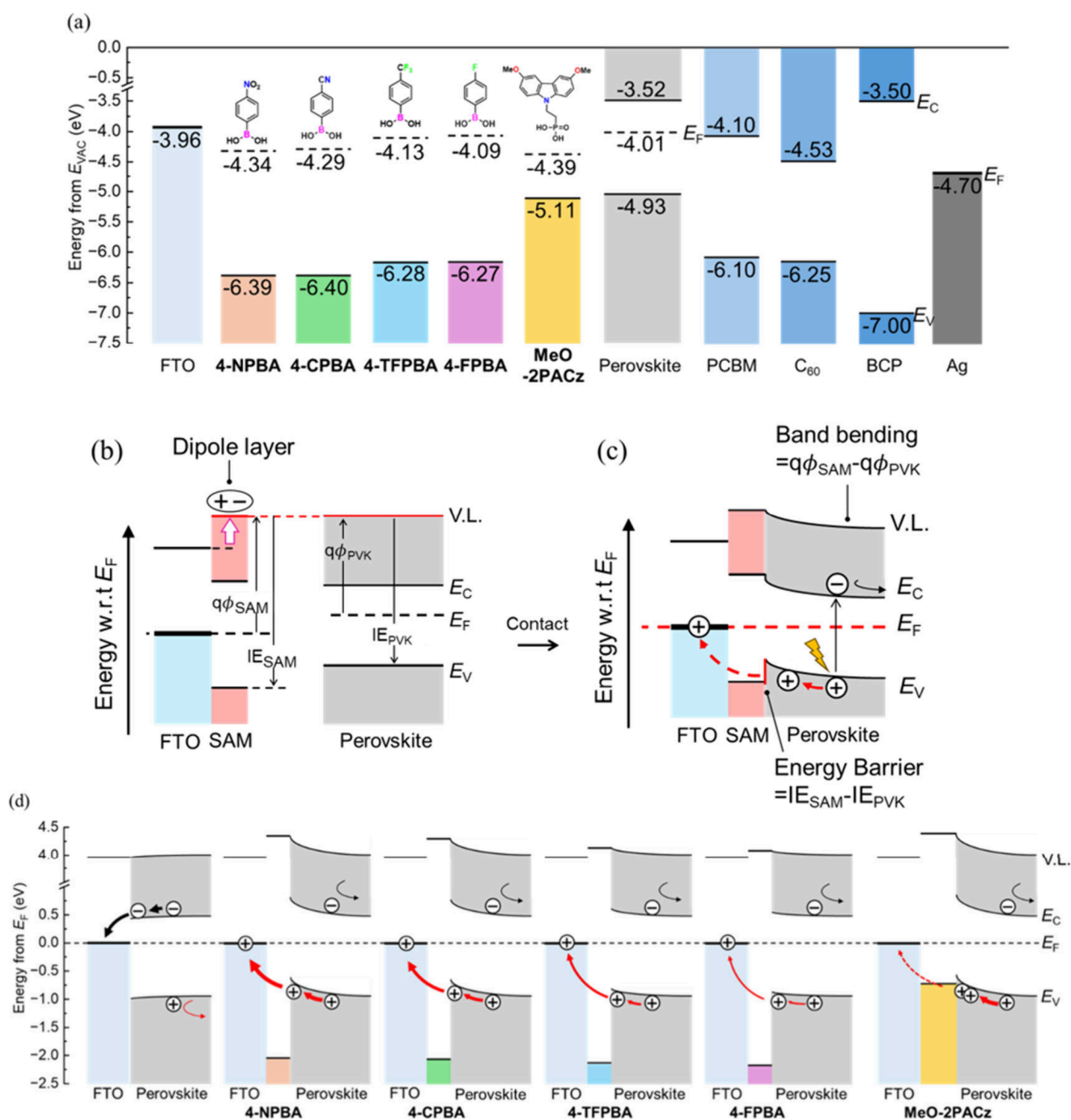


Figure 3. (a) Energy band diagram of PSCs fabricated on various SAM-modified FTO. (b) Energy levels of SAM-modified FTO and perovskite prior to contact. (c) Band alignment after contact based on heterojunction theory. (d) Energy band diagram of FTO/with or without SAM/perovskite interfaces.

perovskite films deposited on various SAM-modified FTO substrates. XPS analysis reveals slight shifts in binding energies depending on the SAM used. For Sn, Pb, and I core levels, the binding energies of perovskite films coated on 4-NPBA-modified FTO are lower compared to those coated on MeO-2PACz-modified FTO. The lower binding energy suggests a reduced electrostatic interaction at the interface, indicating increased electron density around the core levels.⁶⁵

To explain the reason for this huge improvement in PCE, we evaluated the energy level alignment of various components of the PSC. For the construction of the energy band diagram, we performed ultraviolet photoelectron spectroscopy (UPS) measurements to determine the WF and the valence band maxima (VBM) of the SAM-modified FTO substrates (Figure

S7) and the perovskite film deposited on bare FTO (Figure S8). To calculate the VBM of the perovskite, the intensity on the x -axis was plotted on a logarithmic scale as proposed previously.^{66,67} The WFs were determined from the secondary electron cutoff (SECO) region of the UPS spectra (Figure S7a and Figure S8a). In the case of BA-based SAMs these measured WF trends are in good agreement with those determined by Kelvin probe force microscopy (KPFM) (Figure S9 and Table S2). The order of the WF among the BA-based SAMs corresponds to the magnitude of the permanent dipole moments of the isolated molecules. The VBMs were determined from the UPS spectral onset. In the present measurements, a clear spectral onset was observed for MeO-2PACz, whereas the spectral features of the BA-based

SAMs closely resemble those of the bare FTO (Figure S7b). Therefore, the ionization energies of the BA-based SAMs were determined by enlarging the spectral intensity, as shown in Figure S7b. The VBM values determined here are consistent with those obtained by photoemission yield spectroscopy (PYS), as shown in Figure S10. The weak UPS signal from the BA-based SAMs suggests the low adsorption density, which will be discussed later.

The UV–visible spectra and the Tauc plot (Figure S11a,b) for the perovskite films coated on various SAM-modified FTO substrates showed no noticeable change in the absorption onset, thereby maintaining more or less similar band gap energy ($E_g \approx 1.41$ eV). The energy band diagram displayed in Figure 3a was then constructed using the VBM and the WF determined from UPS, E_g determined from the Tauc plot, and the conduction band minimum (CBM) calculated using the formula $\text{CBM} = \text{VBM} + E_g$. The UPS analysis and the energy band diagram show that among the BA-based SAMs used, 4-NPBA exhibited the largest WF, consistent with its large dipole moment. However, the energy band diagram also indicates the formation of an interfacial energy barrier unfavorable for hole collection in the case of all these SAMs, including MeO-2PACz. This can be explained by an energy level alignment model for ITO/SAM/perovskite interfaces based on the semiconductor heterojunction theory⁶⁸ for carbazole-derived SAMs proposed in our previous study⁶⁹ where both the differences in WF and ionization energy are considered to influence hole collection efficiency, as shown in Figure 3b,c. In this model, the FTO/SAM interface is treated as a typical metal/organic interface,⁶⁰ where band bending within the SAM layer is neglected due to its ultrathin nature (approximately 1 nm), rendering such effects insignificant. As discussed earlier, the SAM layer modifies the FTO WF via its intrinsic molecular dipole. Next, we consider the junction between the SAM-coated FTO (the WF, $q\phi_{\text{SAM}}$ and the ionization energy, IE_{SAM}) and the perovskite layer (the WF, $q\phi_{\text{perovskite}}$ and the ionization energy, $\text{IE}_{\text{perovskite}}$) as shown in Figure 3b. After contact is established, the charge carriers are allowed to flow between the layers to reach thermal equilibrium (Figure 3c); the vacuum level alignment is assumed at the interface, and the perovskite energy bands bend to achieve Fermi level alignment across the FTO/SAM/perovskite layers. This model leads to two key outcomes governing the hole collection efficiency: (i) an energy barrier is formed at the interface, corresponding to the difference in ionization energies between the SAM and the perovskite, $\text{IE}_{\text{SAM}} - \text{IE}_{\text{perovskite}}$; and (ii) band bending occurs in the perovskite layer, the magnitude is the difference in WF between the SAM and the perovskite, $q\phi_{\text{SAM}} - q\phi_{\text{perovskite}}$.

According to this model, we constructed the energy level diagram for the FTO/SAM/perovskite interfaces, as shown in Figure 3d. At the FTO/perovskite interface without a SAM, downward band bending toward the interface occurs, which is unfavorable for hole collection. For the FTO/MeO-2PACz/perovskite, the energy barrier is formed which also impedes the hole collection. These predictions agree well with the J_{sc} behaviors. Conversely, in the case of BA-based SAMs, an interfacial energy barrier is unfavorable for hole collection. Specifically, SAMs with $-\text{NO}_2$ and $-\text{CN}$ substituents create the highest barrier, while those with $-\text{F}$ substituents generate the lowest; however, this trend is opposite to the measured J_{sc} and V_{oc} . Interestingly, the variation in J_{sc} as well as V_{oc} correlates instead with the degree of band bending, suggesting

that hole collection is primarily governed by band bending rather than by the height of the interfacial energy barrier in the BA-based SAM system. Therefore, only the band bending appears to impact the solar cell performance, suggesting that the BA-based SAMs primarily act as the WF modifier.

This behavior can be rationalized by two possible scenarios. One is that the hole transport across the SAM layer occurs via quantum tunnelling.⁷⁰ To investigate this hypothesis, we estimated the tunneling probability across the SAM-induced barrier, which requires knowledge of the barrier height, barrier width, and effective hole mass. The barrier height values were obtained experimentally. For the effective mass of the hole, we used a value of $0.25m_0$, which is consistent with reported values for perovskite MAPbI_3 ($m^* = 0.25m_0$)⁶⁷ and similar to the electron effective mass in FTO ($m^* \approx 0.28m_0$).⁷¹ The barrier width was estimated from the molecular length of each SAM species, which was calculated via DFT at the B3LYP/6-31G(d) level, as shown in Figure S12. Using these parameters, the tunneling probabilities were calculated and are summarized in Table S3. In our previous study on carbazole-based SAMs, which had molecular lengths exceeding 1 nm, tunnelling probabilities were limited to only a few percent. This means both the energy barrier and the band bending affects the hole collection efficiency. In contrast, the BA-based SAMs considered here have lengths around 0.8 nm, resulting in significantly higher tunnelling probabilities. Therefore, only the band bending affects the hole collection efficiency. Although the precise molecular orientation on the surface is not yet known, tilting of the molecules would effectively reduce the barrier width further, potentially increasing the tunnelling probability to above 15%.

The other possible explanation is that the substrates are not fully covered by BA-based SAMs, so charge carrier collection occurs directly from the perovskite layer to FTO, rather than through the BA-based SAM layer. In this case, the partially covered BA-based SAMs act as a WF modifier. If the WF is not uniform, the WF obtained from the SECO corresponds to an average of the high and low WF regions.^{72,73} This scenario is supported by the relatively weak intensity of the UPS signal for BA-based SAMs. For further confirmation, we performed the XPS on the N 1s core levels (Figure S13). The peak area shows that the adsorption density of 4-NPBA is approximately one-fourth that of MeO-2PACz. These results indicate that 4-NPBA acts only as a WF modifier, whereas MeO-2PACz acts as a WF modifier and an HTL both. In any case, these SAMs induce an interfacial electric field that results in upward band bending in the adjacent perovskite layer, thus energetically favoring hole collection, while simultaneously repelling electrons and minimizing interfacial recombination.

To investigate the influence of SAMs on charge extraction, we performed transient absorption (TA) measurements on perovskite films deposited on glass and FTO substrates modified with various BA-based SAMs, including 4-NPBA, 4-CPBA, 4-TFPBA, 4-FPBA, and MeO-2PACz.^{74,75} Figure S14 shows the TA spectra for various perovskite films coated on a glass substrate and various SAM-modified FTO substrates. It is evident that the perovskite films deposited on SAM-modified FTO substrates exhibit a faster decay of the Ground State Bleach (GSB) signal compared those deposited on glass substrates, indicating more efficient charge extraction by improved interfacial energy alignment. The kinetic traces extracted from the GSB were normalized and then fitted by using a biexponential decay function: $y = A_1 e^{-x/\tau_1} + A_2 e^{-x/\tau_2} +$

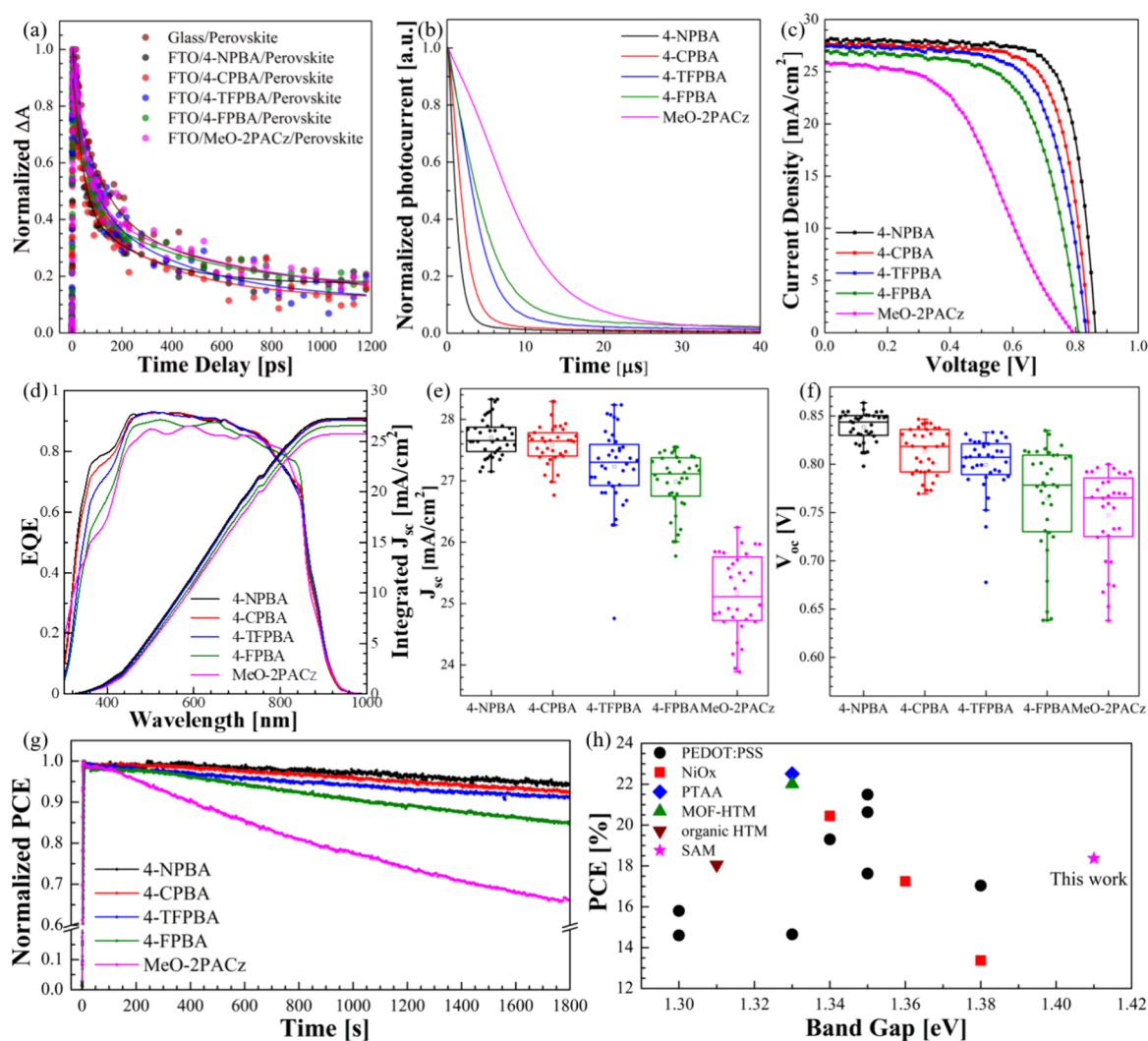


Figure 4. (a) Biexponential kinetic decay traces for perovskite films deposited on various SAM-modified FTO. (b) Transient photocurrent decay (TPC) spectra, and (c) current–voltage (I – V) spectra under reverse scan – for the PSCs fabricated on various SAM-modified FTO substrates. (d) EQE for the PSCs measured under monochromatic light illumination. Box chart showing (e) J_{sc} and (f) V_{oc} of 18 independent PSCs. (g) Maximum power point tracking (MPPT) of the PSCs fabricated on various SAM-modified FTO. (h) The PCEs of state-of-the-art Sn–Pb PSCs with band gap ranging from 1.3–1.4 eV reported in the literature. 1.3 eV: 14.6%,⁷⁷ 15.8%;⁷⁸ 1.31 eV: 18.05%;⁵⁶ 1.33 eV: 14.65%;⁷⁹ 22.01%;⁵⁵ 22.51%;⁵⁷ 1.34 eV: 19.3%;⁸⁰ 20.45%;⁵⁸ 1.35 eV: 17.63%;⁸¹ 20.63%;⁸² 21.49%;⁷⁶ 1.36 eV: 17.25%;⁸³ 1.38 eV: 13.37%,⁸⁴ 17.04%.⁷⁹

y_0 , as shown in Figure 4a. The kinetic parameters obtained after fitting the kinetic traces as well as decay rates (k_{decay}) and hole extraction rate (k_{ext}) calculated therefrom is summarized in Table S4. The glass/perovskite sample, devoid of the SAM layer, served as the reference to evaluate the intrinsic recombination lifetime of the perovskite layer. The decay for this sample arises primarily from bulk and surface recombination processes, as there is no interface to facilitate charge extraction. The amplitude-weighted average lifetime (τ) of the glass/perovskite sample calculated using the formula $\tau = \frac{A_1\tau_1^2 + A_2\tau_2^2}{A_1\tau_1 + A_2\tau_2}$ was found to be 949.14 ps. Similarly, the perovskite films coated on FTO substrate modified by 4-NPBA, 4-CPBA, 4-TFPBA, 4-FPBA, and MeO-2PACz exhibited $\langle\tau\rangle$ values of 209.26, 298.93, 362.86, 377.53, and 499.78 ps, respectively. Further, decay rates (k_{decay}) were determined using the formula $k_{decay} = 1/\langle\tau\rangle$, where the perovskite films coated on glass, FTO-modified by 4-NPBA, 4-CPBA, 4-TFPBA, 4-FPBA, and MeO-2PACz, exhibited k_{decay} values of 1.05×10^{-3} , 4.78×10^{-3} , 3.35

$\times 10^{-3}$, 2.5×10^{-3} , 2.65×10^{-3} , and 2.00×10^{-3} ps⁻¹, respectively. The perovskite films deposited on various SAM-modified FTO substrates showed shorter average lifetimes and significantly faster decay rates ($k_{decay,SAM}$) compared to those deposited on glass ($k_{decay,perovskite}$), indicating the presence of efficient interfacial hole extraction pathways. Assuming the perovskite remains the same for both glass and SAM-modified samples and the only difference is the presence of the SAM, the additional decay can be attributed to hole transfer. The hole extraction rate (k_{ext}), calculated using the formula $k_{ext} = k_{decay,SAM} - k_{decay,perovskite}$ follows the order 3.73×10^{-3} ps⁻¹ (FTO/4-NPBA/Perovskite), 2.29×10^{-3} ps⁻¹ (FTO/4-CPBA/Perovskite), 1.70×10^{-3} ps⁻¹ (FTO/4-TFPBA/Perovskite), 1.60×10^{-3} ps⁻¹ (FTO/4-FPBA/Perovskite), 0.95×10^{-3} ps⁻¹ (FTO/MeO-2PACz/Perovskite). Further validation of these results was conducted by transient photocurrent decay (TPC) analyses (Figure 4b and Table S5). In order to isolate the contribution of SAM on the charge transport time ($t_{TPC,tr}$), the device architecture, namely, FTO, perovskite, ETL, and

silver (Ag) electrode, were kept identical while only the SAM was varied. The fabricated solar cells were operated under short-circuit conditions. $t_{\text{TPC, tr}}$ defined as the time interval during which transport time decayed to $1/e$ of the initial values, was calculated after fitting of the TPC curves. The $t_{\text{TPC, tr}}$ followed the order $1.18 \mu\text{s}$ (FTO/4-NPBA/Perovskite), $2.01 \mu\text{s}$ (FTO/4-CPBA/Perovskite), $3.85 \mu\text{s}$ (FTO/4-TFPBA/Perovskite), $4.71 \mu\text{s}$ (FTO/4-FPBA/Perovskite), and $10.58 \mu\text{s}$ (FTO/MeO-2PACz/Perovskite). Therefore, the results from TA and TPC validate our previous findings that the BA-based SAMs facilitate smooth transport of holes when compared with their MeO-2PACz counterparts.

To verify the obtained results from various characterizations, photovoltaic performance of various PSCs fabricated on different SAM-modified FTO substrates was investigated. Figure 4c shows the I - V spectra for various SAM-based PSCs measured under a reverse scan after illumination with a simulated solar irradiation of $100 \text{ mW}/\text{cm}^2$. The I - V spectra for the same PSCs under both forward and reverse scans are shown in Figure S15. Similarly, Figure 4d shows the external quantum efficiency (EQE) spectra that were obtained after the PSCs were illuminated with monochromatic light. The PSC fabricated on 4-NPBA-modified FTO exhibited the best PCE of 18.37% along with a J_{sc} of $27.88 \text{ mA}/\text{cm}^2$, a V_{oc} of 0.864 V, and an FF of 0.76. In contrast, devices fabricated on MeO-2PACz exhibited a much lower PCE of 9.27%, along with a J_{sc} of $25.85 \text{ mA}/\text{cm}^2$, V_{oc} of 0.79 V, and an FF of 0.45. The PSCs fabricated using BA-based SAMs achieved excellent J_{sc} values in the range of 26.7 – $27.9 \text{ mA}/\text{cm}^2$, which are consistent with the J_{sc} values reported for Sn–Pb PSCs with similar band gaps.^{58,76} The superior photovoltaic performance of 4-NPBA-based PSCs can be ascribed to the improved film quality and better hole transport aided by pronounced band bending at the SAM/perovskite interface. The poor photovoltaic performance of MeO-2PACz-based PSCs even after substantial band bending at the SAM/perovskite interface can be attributed to the interfacial energy barrier formed at the interface, thus leading to substantial recombination and less efficient charge transport. Further, the minimal possibility of both tunneling through the MeO-2PACz SAM and direct hole transport from the perovskite to the FTO, owing to its longer molecular length and uniform surface coverage, makes hole transport more difficult. As a result, the PSCs fabricated on other BA-based SAM-modified FTO substrates also demonstrated better photovoltaic performance compared to the MeO-2PACz-based device, despite exhibiting negligible differences in perovskite film quality. The external quantum efficiency (EQE) spectra for BA-based SAMs shows that the EQE notably increased in the 350–500 nm range, signifying increased hole carrier transport and collection. The photovoltaic parameters of the best-performing PSCs fabricated on various SAM-modified FTO substrates are tabulated in Table S6. Additionally, the solar cell parameters of 18 independent PSCs fabricated on various SAM-modified FTO substrates are summarized in the box plots in Figure 4e,f and Figure S16a–d. The box plots show that 4-NPBA-modified FTO-based PSCs demonstrated the best performance, with the highest average J_{sc} , FF, and V_{oc} thus resulting in a highest PCE. This superior performance correlates with its large WF and pronounced band bending at the SAM/perovskite interface, facilitating efficient hole extraction. In contrast, MeO-2PACz-based devices exhibit the lowest performance across all parameters, highlighting the advantage of BA-based SAMs in improving interfacial

energetics and charge extraction. Figure 4g presents the normalized short-term (30 min) maximum power point tracking (MPPT) of various SAM-based PSCs measured inside a glovebox under nitrogen atmosphere. The PSCs based on 4-NPBA-modified FTO exhibited better photostability, indicating superior interfacial stability between the perovskite and the SAM-modified FTO. In contrast, PSCs incorporating MeO-2PACz showed comparatively poorer photostability, likely due to reduced interfacial stability. Figure 4h summarizes the PCEs of state-of-the-art ideal band gap PSCs (1.3–1.4 eV) reported in recent years and the PCE obtained in this work.

This study highlights the role of BA-based SAMs in enhancing the photovoltaic performance of ideal band gap Sn–Pb PSCs by modulating interfacial energetics. Although these SAMs exhibit an unfavorable energy-level offset for hole collection at the SAM/perovskite interface, they achieved better photovoltaic performance compared to MeO-2PACz, with PSCs fabricated on 4-NPBA-modified FTO achieving the best PCE. This improvement is attributed to interfacial band bending-assisted tunneling of holes through the BA-based SAM layer, facilitated by their short molecular lengths and high tunneling probabilities, as supported by DFT calculations. In addition, the relatively lower surface coverage of BA-based SAMs on FTO substrates (as indicated by XPS analysis) allows partial direct hole transport from the perovskite layer to the FTO. In such case, BA-based SAMs primarily functions as a WF modifier. In contrast, although MeO-2PACz induces favorable band bending at the FTO/MeO-2PACz/perovskite interface, the combination of an interfacial energy barrier for hole collection and lower tunneling probability results in poorer device performance. The better PCE of PSCs fabricated on 4-NPBA-modified FTO substrates compared to their MeO-2PACz counterparts was further validated by TA and TPC measurements where PSCs fabricated on 4-NPBA exhibited the highest hole-extraction rate ($k_{\text{ext}} = 3.73 \times 10^{-3} \text{ ps}^{-1}$) and the shortest charge-transport time ($t_{\text{TPC, tr}} = 1.18 \mu\text{s}$).

■ ASSOCIATED CONTENT

SI Supporting Information

The Supporting Information is available free of charge at <https://pubs.acs.org/doi/10.1021/acsenenergylett.5c01900>.

Description of perovskite precursor solution preparation, solar cell fabrication procedure, and characterization methods; molecular structures of SAMs; Gaussian optimized structure and electrostatic potential map of MeO-2PACz; XPS; IR; AFM; UPS; surface potential maps (KPFM); PYS; UV–visible spectra; Tauc plot; TA spectra; box plot of various photovoltaic parameters; thickness of the perovskite film; SEM; Urbach energy; water contact angle of SAM-modified FTO substrates (PDF)

■ AUTHOR INFORMATION

Corresponding Authors

Safalmani Pradhan – *Info-Powered Energy System Research Center, The University of Electro-Communications, Chofu, Tokyo 182-8585, Japan*; orcid.org/0009-0004-0382-6518; Email: safalmani@uec.ac.jp

Jiaqi Liu – *Info-Powered Energy System Research Center, The University of Electro-Communications, Chofu, Tokyo 182-8585, Japan*; Email: liujiaqi@uec.ac.jp

Qing Shen – Info-Powered Energy System Research Center, The University of Electro-Communications, Chofu, Tokyo 182-8585, Japan; Graduate School of Informatics and Engineering, The University of Electro-Communications, Chofu, Tokyo 182-8585, Japan; orcid.org/0000-0001-8359-3275; Email: shen@pc.uec.ac.jp

Shuzi Hayase – Info-Powered Energy System Research Center, The University of Electro-Communications, Chofu, Tokyo 182-8585, Japan; orcid.org/0000-0001-8192-5336; Email: hayase@uec.ac.jp

Authors

Huān Bi – Info-Powered Energy System Research Center, The University of Electro-Communications, Chofu, Tokyo 182-8585, Japan

Gaurav Kapil – Info-Powered Energy System Research Center, The University of Electro-Communications, Chofu, Tokyo 182-8585, Japan; orcid.org/0000-0002-5066-4978

Aruto Akatsuka – Graduate School of Engineering, Chiba University, 263-8522 Chiba, Japan

Ajay Kumar Baranwal – Department of Electronics and Communications Engineering, Madan Mohan Malaviya University of Technology, Gorakhpur, Uttar Pradesh 273010, India; orcid.org/0000-0003-4582-4532

Dandan Wang – Graduate School of Informatics and Engineering, The University of Electro-Communications, Chofu, Tokyo 182-8585, Japan

Dong Liu – Graduate School of Informatics and Engineering, The University of Electro-Communications, Chofu, Tokyo 182-8585, Japan

Suraya Shaban – Info-Powered Energy System Research Center, The University of Electro-Communications, Chofu, Tokyo 182-8585, Japan

Takeshi Kitamura – Info-Powered Energy System Research Center, The University of Electro-Communications, Chofu, Tokyo 182-8585, Japan; orcid.org/0009-0005-2782-4549

Shahrir Razey Sahamir – Info-Powered Energy System Research Center, The University of Electro-Communications, Chofu, Tokyo 182-8585, Japan; orcid.org/0000-0002-9167-5980

Yasuhiro Fujiwara – Info-Powered Energy System Research Center, The University of Electro-Communications, Chofu, Tokyo 182-8585, Japan

Hiroshi Segawa – Department of General Systems Studies, Graduate School of Arts and Sciences, The University of Tokyo, Meguro-ku, Tokyo 153-8902, Japan; orcid.org/0000-0001-8076-9722

Hiroyuki Yoshida – Graduate School of Engineering, Chiba University, 263-8522 Chiba, Japan; orcid.org/0000-0002-8889-324X

Complete contact information is available at:

<https://pubs.acs.org/10.1021/acsenerylett.5c01900>

Author Contributions

S.P. contributed by Conceptualization, Methodology, Investigation, Formal Analysis, Writing – Original Draft, Writing – Review & Editing; Visualization and Data Curation. H.B. contributed by Methodology, Investigation and Formal Analysis. G.K. contributed by Methodology, Formal Analysis and Visualization; A.A. contributed by Investigation, Formal Analysis, Writing – Original Draft and Visualization. A.K.B., D.W., D.L., S.S., T.K., S.R.S., and Y.F. contributed by Formal

Analysis and Writing – Review and Editing. J.L. contributed by Formal Analysis, Writing – Original Draft, Writing – Review & Editing and Visualization. H.S. contributed by Conceptualization, Writing – Review & Editing. H.Y. contributed by Formal Analysis, Writing – Original Draft, Writing – Review & Editing, and Visualization. Q.S. contributed by Conceptualization, Formal Analysis, Writing – Review & Editing and Supervision. S.H. contributed by Conceptualization, Formal Analysis, Writing – Review & Editing, Visualization, Supervision, Project administration, Resources, Fund Acquisition and Data Curation.

Notes

The authors declare no competing financial interest.

REFERENCES

- (1) Kojima, A.; Teshima, K.; Shirai, Y.; Miyasaka, T. Organometal Halide Perovskites as Visible-Light Sensitizers for Photovoltaic Cells. *J. Am. Chem. Soc.* **2009**, *131* (17), 6050–6051.
- (2) Burschka, J.; Pellet, N.; Moon, S.-J.; Humphry-Baker, R.; Gao, P.; Nazeeruddin, M. K.; Grätzel, M. Sequential Deposition as a Route to High-Performance Perovskite-Sensitized Solar Cells. *Nature* **2013**, *499* (7458), 316–319.
- (3) Liu, M.; Johnston, M. B.; Snaith, H. J. Efficient Planar Heterojunction Perovskite Solar Cells by Vapour Deposition. *Nature* **2013**, *501* (7467), 395–398.
- (4) Green, M. A.; Dunlop, E. D.; Yoshita, M.; Kopidakis, N.; Bothe, K.; Siefert, G.; Hao, X.; Jiang, J. Y. Solar Cell Efficiency Tables (Version 66). *Prog. Photovoltaics Res. Appl.* **2025**, *33* (7), 795–810.
- (5) Wang, Y.; Zhang, Y.; Zhang, P.; Zhang, W. High Intrinsic Carrier Mobility and Photon Absorption in the Perovskite CH₃NH₃PbI₃. *Phys. Chem. Chem. Phys.* **2015**, *17* (17), 11516–11520.
- (6) Li, Z.; Zhao, Y.; Wang, X.; Sun, Y.; Zhao, Z.; Li, Y.; Zhou, H.; Chen, Q. Cost Analysis of Perovskite Tandem Photovoltaics. *Joule* **2018**, *2* (8), 1559–1572.
- (7) Wang, P.; Wu, Y.; Cai, B.; Ma, Q.; Zheng, X.; Zhang, W.-H. Solution-Processable Perovskite Solar Cells toward Commercialization: Progress and Challenges. *Adv. Funct. Mater.* **2019**, *29* (47), 1807661.
- (8) Wang, S.; Li, M.-H.; Jiang, Y.; Hu, J.-S. Instability of Solution-Processed Perovskite Films: Origin and Mitigation Strategies. *Mater. Futur.* **2023**, *2* (1), 012102.
- (9) Meredith, P.; Armin, A. Scaling of next Generation Solution Processed Organic and Perovskite Solar Cells. *Nat. Commun.* **2018**, *9* (1), 5261.
- (10) Chen, J.; Park, N. Causes and Solutions of Recombination in Perovskite Solar Cells. *Adv. Mater.* **2019**, *31* (47), 1803019.
- (11) Ye, Y.; Chen, L.; Chen, X.; Ma, C.; Lv, B.; Wang, J.; Dou, W.; Zhang, C.; Ma, T.; Tang, J. Interfacial Energy Level Alignment and Defect Passivation by Using a Multifunctional Molecular for Efficient and Stable Perovskite Solar Cells. *Adv. Funct. Mater.* **2024**, *34* (8), 2310136.
- (12) Yang, B.; Suo, J.; Di Giacomo, F.; Olthof, S.; Bogachuk, D.; Kim, Y.; Sun, X.; Wagner, L.; Fu, F.; Zakeeruddin, S. M.; Hinsch, A.; Grätzel, M.; Di Carlo, A.; Hagfeldt, A. Interfacial Passivation Engineering of Perovskite Solar Cells with Fill Factor over 82% and Outstanding Operational Stability on N-i-p Architecture. *ACS Energy Lett.* **2021**, *6* (11), 3916–3923.
- (13) Zhang, Z.; Qiao, L.; Meng, K.; Long, R.; Chen, G.; Gao, P. Rationalization of Passivation Strategies toward High-Performance Perovskite Solar Cells. *Chem. Soc. Rev.* **2023**, *52* (1), 163–195.
- (14) Xia, Y.; Yan, G.; Lin, J. Review on Tailoring PEDOT:PSS Layer for Improved Device Stability of Perovskite Solar Cells. *Nanomaterials* **2021**, *11* (11), 3119.
- (15) Cameron, J.; Skabara, P. J. The Damaging Effects of the Acidity in PEDOT:PSS on Semiconductor Device Performance and Solutions Based on Non-Acidic Alternatives. *Mater. Horizons* **2020**, *7* (7), 1759–1772.

- (16) Lee, Y.; Biswas, S.; Kim, H. Effect of Hygroscopicity of the Hole Transport Layer on the Stability of Organic Solar Cells. *Thin Solid Films* **2022**, *746*, 139134.
- (17) Liu, S.; Li, J.; Xiao, W.; Chen, R.; Sun, Z.; Zhang, Y.; Lei, X.; Hu, S.; Kober-Czerny, M.; Wang, J.; Ren, F.; Zhou, Q.; Raza, H.; Gao, Y.; Ji, Y.; Li, S.; Li, H.; Qiu, L.; Huang, W.; Zhao, Y.; Xu, B.; Liu, Z.; Snaith, H. J.; Park, N.-G.; Chen, W. Buried Interface Molecular Hybrid for Inverted Perovskite Solar Cells. *Nature* **2024**, *632* (8025), 536–542.
- (18) Dai, Z.; Yadavalli, S. K.; Chen, M.; Abbaspourtamijani, A.; Qi, Y.; Padture, N. P. Interfacial Toughening with Self-Assembled Monolayers Enhances Perovskite Solar Cell Reliability. *Science* **2021**, *372* (6542), 618–622.
- (19) Zuo, L.; Gu, Z.; Ye, T.; Fu, W.; Wu, G.; Li, H.; Chen, H. Enhanced Photovoltaic Performance of CH₃NH₃PbI₃ Perovskite Solar Cells through Interfacial Engineering Using Self-Assembling Monolayer. *J. Am. Chem. Soc.* **2015**, *137* (7), 2674–2679.
- (20) Li, M.; Liu, M.; Qi, F.; Lin, F. R.; Jen, A. K.-Y. Self-Assembled Monolayers for Interfacial Engineering in Solution-Processed Thin-Film Electronic Devices: Design, Fabrication, and Applications. *Chem. Rev.* **2024**, *124* (5), 2138–2204.
- (21) Jiang, T.; Yang, Y.; Hao, X.; Fan, J.; Wu, L.; Wang, W.; Zeng, G.; Halim, M. A.; Zhang, J. Self-Assembled Monolayer Hole Transport Layers for High-Performance and Stable Inverted Perovskite Solar Cells. *Energy Fuels* **2024**, *38* (21), 21371–21381.
- (22) Almasabi, K.; Zheng, X.; Turedi, B.; Alsalloum, A. Y.; Lintangpradipto, M. N.; Yin, J.; Gutiérrez-Arzaluz, L.; Kotsovos, K.; Jamal, A.; Gereige, I.; Mohammed, O. F.; Bakr, O. M. Hole-Transporting Self-Assembled Monolayer Enables Efficient Single-Crystal Perovskite Solar Cells with Enhanced Stability. *ACS Energy Lett.* **2023**, *8* (2), 950–956.
- (23) Jiang, Q.; Tirawat, R.; Kerner, R. A.; Gaulding, E. A.; Xian, Y.; Wang, X.; Newkirk, J. M.; Yan, Y.; Berry, J. J.; Zhu, K. Towards Linking Lab and Field Lifetimes of Perovskite Solar Cells. *Nature* **2023**, *623* (7986), 313–318.
- (24) Kapil, G.; Bessho, T.; Sanehira, Y.; Sahamir, S. R.; Chen, M.; Baranwal, A. K.; Liu, D.; Sono, Y.; Hirotsu, D.; Nomura, D.; Nishimura, K.; Kamarudin, M. A.; Shen, Q.; Segawa, H.; Hayase, S. Tin-Lead Perovskite Solar Cells Fabricated on Hole Selective Monolayers. *ACS Energy Lett.* **2022**, *7* (3), 966–974.
- (25) Liu, W.; Zang, Y.; Tu, Y.; Wang, Y.; Zhu, Z.; Zhu, C.; Yan, W. Reconstruction of Hole Transport Layer via Co-Self-Assembled Molecules for High-Performance Inverted Perovskite Solar Cells. *Small* **2025**, *21* (3), 2408314.
- (26) Roe, J.; Son, J. G.; Park, S.; Seo, J.; Song, T.; Kim, J.; Oh, S. O.; Jo, Y.; Lee, Y.; Shin, Y. S.; Jang, H.; Lee, D.; Yuk, D.; Seol, J. G.; Kim, Y. S.; Cho, S.; Kim, D. S.; Kim, J. Y. Synergistic Buried Interface Regulation of Tin-Lead Perovskite Solar Cells via Co-Self-Assembled Monolayers. *ACS Nano* **2024**, *18* (35), 24306–24316.
- (27) Dong, B.; Wei, M.; Li, Y.; Yang, Y.; Ma, W.; Zhang, Y.; Ran, Y.; Cui, M.; Su, Z.; Fan, Q.; Bi, Z.; Edvinsson, T.; Ding, Z.; Ju, H.; You, S.; Zakeeruddin, S. M.; Li, X.; Hagfeldt, A.; Grätzel, M.; Liu, Y. Self-Assembled Bilayer for Perovskite Solar Cells with Improved Tolerance against Thermal Stresses. *Nat. Energy* **2025**, *10* (3), 342–353.
- (28) Zhang, S.; Wu, R.; Mu, C.; Wang, Y.; Han, L.; Wu, Y.; Zhu, W.-H. Conjugated Self-Assembled Monolayer as Stable Hole-Selective Contact for Inverted Perovskite Solar Cells. *ACS Mater. Lett.* **2022**, *4* (10), 1976–1983.
- (29) Li, C.; Zhang, Z.; Zhang, H.; Yan, W.; Li, Y.; Liang, L.; Yu, W.; Yu, X.; Wang, Y.; Yang, Y.; Nazeeruddin, M. K.; Gao, P. Fully Aromatic Self-Assembled Hole-Selective Layer toward Efficient Inverted Wide-Bandgap Perovskite Solar Cells with Ultraviolet Resistance. *Angew. Chemie Int. Ed.* **2024**, *63* (1), No. e202315281.
- (30) Song, D.; Ramakrishnan, S.; Zhang, Y.; Yu, Q. Mixed Self-Assembled Monolayers for High-Photovoltage Tin Perovskite Solar Cells. *ACS Energy Lett.* **2024**, *9* (4), 1466–1472.
- (31) He, D.; Chen, P.; Steele, J. A.; Wang, Z.; Xu, H.; Zhang, M.; Ding, S.; Zhang, C.; Lin, T.; Kremer, F.; Xu, H.; Hao, M.; Wang, L. Homogeneous 2D/3D Heterostructured Tin Halide Perovskite Photovoltaics. *Nat. Nanotechnol.* **2025**, *20* (6), 779–786.
- (32) Shockley, W.; Queisser, H. J. Detailed Balance Limit of Efficiency of P-n Junction Solar Cells. *J. Appl. Phys.* **1961**, *32* (3), 510–519.
- (33) Rühle, S. Tabulated Values of the Shockley-Queisser Limit for Single Junction Solar Cells. *Sol. Energy* **2016**, *130*, 139–147.
- (34) Ali, F.; Roldán-Carmona, C.; Sohail, M.; Nazeeruddin, M. K. Applications of Self-Assembled Monolayers for Perovskite Solar Cells Interface Engineering to Address Efficiency and Stability. *Adv. Energy Mater.* **2020**, *10* (48), 2002989.
- (35) Shi, Z.-E.; Cheng, T.-H.; Lung, C.-Y.; Lin, C.-W.; Wang, C.-L.; Jiang, B.-H.; Hsiao, Y.-S.; Chen, C.-P. Achieving over 42% Indoor Efficiency in Wide-Bandgap Perovskite Solar Cells through Optimized Interfacial Passivation and Carrier Transport. *Chem. Eng. J.* **2024**, *498*, 155512.
- (36) Lim, K.-G.; Ahn, S.; Lee, T.-W. Energy Level Alignment of Dipolar Interface Layer in Organic and Hybrid Perovskite Solar Cells. *J. Mater. Chem. C* **2018**, *6* (12), 2915–2924.
- (37) Al-Ashouri, A.; Marčinkas, M.; Kasparavičius, E.; Malinauskas, T.; Palmstrom, A.; Getautis, V.; Albrecht, S.; McGehee, M. D.; Magomedov, A. Wettability Improvement of a Carbazole-Based Hole-Selective Monolayer for Reproducible Perovskite Solar Cells. *ACS Energy Lett.* **2023**, *8* (2), 898–900.
- (38) Gelmetti, I.; Montcada, N. F.; Pérez-Rodríguez, A.; Barrera, E.; Ocal, C.; García-Benito, I.; Molina-Ontoria, A.; Martín, N.; Vidal-Ferran, A.; Palomares, E. Energy Alignment and Recombination in Perovskite Solar Cells: Weighted Influence on the Open Circuit Voltage. *Energy Environ. Sci.* **2019**, *12* (4), 1309–1316.
- (39) Al-Ashouri, A.; Magomedov, A.; Roß, M.; Jošt, M.; Talaikis, M.; Chistiakova, G.; Bertram, T.; Márquez, J. A.; Köhnen, E.; Kasparavičius, E.; Levenco, S.; Gil-Escrig, L.; Hages, C. J.; Schlattmann, R.; Rech, B.; Malinauskas, T.; Unold, T.; Kaufmann, C. A.; Korte, L.; Niaura, G.; Getautis, V.; Albrecht, S. Conformal Monolayer Contacts with Lossless Interfaces for Perovskite Single Junction and Monolithic Tandem Solar Cells. *Energy Environ. Sci.* **2019**, *12* (11), 3356–3369.
- (40) Park, S. M.; Wei, M.; Lempesis, N.; Yu, W.; Hossain, T.; Agosta, L.; Carnevali, V.; Atapattu, H. R.; Serles, P.; Eickemeyer, F. T.; Shin, H.; Vafaie, M.; Choi, D.; Darabi, K.; Jung, E. D.; Yang, Y.; Kim, D. B.; Zakeeruddin, S. M.; Chen, B.; Amassian, A.; Filleter, T.; Kanatzidis, M. G.; Graham, K. R.; Xiao, L.; Rothlisberger, U.; Grätzel, M.; Sargent, E. H. Low-Loss Contacts on Textured Substrates for Inverted Perovskite Solar Cells. *Nature* **2023**, *624* (7991), 289–294.
- (41) Chen, Q.; Wang, C.; Li, Y.; Chen, L. Interfacial Dipole in Organic and Perovskite Solar Cells. *J. Am. Chem. Soc.* **2020**, *142* (43), 18281–18292.
- (42) Zhang, C.; Kong, W.; Wu, T.; Lin, X.; Wu, Y.; Nakazaki, J.; Segawa, H.; Yang, X.; Zhang, Y.; Wang, Y.; Han, L. Reduction of Nonradiative Loss in Inverted Perovskite Solar Cells by Donor- π -Acceptor Dipoles. *ACS Appl. Mater. Interfaces* **2021**, *13* (37), 44321–44328.
- (43) Gao, K.; Gao, L.; Wang, Q.; Chang, Y.; Zhang, Q.; Zhao, Y.; Tang, Q. Interfacial Dipole Engineering in All-Inorganic Perovskite Solar Cells. *Chem. Commun.* **2023**, *59* (81), 12112–12115.
- (44) Gregori, L.; Meggiolaro, D.; De Angelis, F. Quantifying the Effect of Interfacial Dipoles on the Energy Level Alignment of Metal-Halide Perovskites. *ACS Energy Lett.* **2024**, *9* (11), 5329–5333.
- (45) Xu, C.; Hang, P.; Kan, C.; Guo, X.; Song, X.; Xu, C.; You, G.; Liao, W.-Q.; Zhu, H.; Wang, D.; Chen, Q.; Hong, Z.; Xiong, R.-G.; Yu, X.; Zuo, L.; Chen, H. Molecular Ferroelectric Self-Assembled Interlayer for Efficient Perovskite Solar Cells. *Nat. Commun.* **2025**, *16* (1), 835.
- (46) Rusu, P. C.; Giovannetti, G.; Brocks, G. Dipole Formation at Interfaces of Alkanethiolate Self-Assembled Monolayers and Ag(111). *J. Phys. Chem. C* **2007**, *111* (39), 14448–14456.
- (47) Hofmann, O. T.; Glowatzki, H.; Bürker, C.; Rangger, G. M.; Bröker, B.; Niederhausen, J.; Hosokai, T.; Salzmann, I.; Blum, R.-P.; Rieger, R.; Vollmer, A.; Rajput, P.; Gerlach, A.; Müllen, K.; Schreiber,

- F.; Zojer, E.; Koch, N.; Duhm, S. Orientation-Dependent Work-Function Modification Using Substituted Pyrene-Based Acceptors. *J. Phys. Chem. C* **2017**, *121* (44), 24657–24668.
- (48) Asyuda, A.; Gärtner, M.; Wan, X.; Burkhart, I.; Saßmannshausen, T.; Terfort, A.; Zharnikov, M. Self-Assembled Monolayers with Embedded Dipole Moments for Work Function Engineering of Oxide Substrates. *J. Phys. Chem. C* **2020**, *124* (16), 8775–8785.
- (49) Suo, J.; Yang, B.; Bogachuk, D.; Boschloo, G.; Hagfeldt, A. The Dual Use of SAM Molecules for Efficient and Stable Perovskite Solar Cells. *Adv. Energy Mater.* **2025**, *15* (2), 2400205.
- (50) Wang, Q.; Chueh, C.; Zhao, T.; Cheng, J.; Eslamian, M.; Choy, W. C. H.; Jen, A. K. -Y. Effects of Self-Assembled Monolayer Modification of Nickel Oxide Nanoparticles Layer on the Performance and Application of Inverted Perovskite Solar Cells. *ChemSusChem* **2017**, *10* (19), 3794–3803.
- (51) Peng, Y.; Chen, Y.; Zhou, J.; Luo, C.; Tang, W.; Duan, Y.; Wu, Y.; Peng, Q. Enlarging Moment and Regulating Orientation of Buried Interfacial Dipole for Efficient Inverted Perovskite Solar Cells. *Nat. Commun.* **2025**, *16* (1), 1252.
- (52) Wang, G.; Wang, D.; Chang, J.; Meng, F.; Xiang, W. Dipolar Interlayers in Perovskite Solar Cells. *Sol. RRL* **2023**, *7* (20), 2300481.
- (53) Kırbıyık Kurukavak, Ç.; Yılmaz, T.; Büyükbekar, A.; Kuş, M. Effect of Different Terminal Groups of Phenyl Boronic Acid Self-Assembled Monolayers on the Photovoltaic Performance of Organic Solar Cells. *Opt. Mater. (Amst.)* **2021**, *112*, 110783.
- (54) Akın Kara, D.; Kara, K.; Oylumluoğlu, G.; Yigit, M. Z.; Can, M.; Kim, J. J.; Burnett, E. K.; Gonzalez Arellano, D. L.; Buyukcelebi, S.; Ozel, F.; Usluer, O.; Brisenno, A. L.; Kus, M. Enhanced Device Efficiency and Long-Term Stability via Boronic Acid-Based Self-Assembled Monolayer Modification of Indium Tin Oxide in a Planar Perovskite Solar Cell. *ACS Appl. Mater. Interfaces* **2018**, *10* (35), 30000–30007.
- (55) Cao, J.; Liu, C.-K.; Piradi, V.; Loi, H.-L.; Wang, T.; Cheng, H.; Zhu, X.; Yan, F. Ultrathin Self-Assembly Two-Dimensional Metal-Organic Framework Films as Hole Transport Layers in Ideal-Bandgap Perovskite Solar Cells. *ACS Energy Lett.* **2022**, *7* (10), 3362–3369.
- (56) Guo, H.; Zhang, H.; Liu, S.; Zhang, D.; Wu, Y.; Zhu, W.-H. Efficient and Stable Methylammonium-Free Tin-Lead Perovskite Solar Cells with Hexaazatrinaphthylene-Based Hole-Transporting Materials. *ACS Appl. Mater. Interfaces* **2022**, *14* (5), 6852–6858.
- (57) Liang, Z.; Xu, H.; Zhang, Y.; Liu, G.; Chu, S.; Tao, Y.; Xu, X.; Xu, S.; Zhang, L.; Chen, X.; Xu, B.; Xiao, Z.; Pan, X.; Ye, J. A Selective Targeting Anchor Strategy Affords Efficient and Stable Ideal-Bandgap Perovskite Solar Cells. *Adv. Mater.* **2022**, *34* (18), 2110241.
- (58) Cao, J.; Liu, C.; Xu, Y.; Loi, H.; Wang, T.; Li, M. G.; Liu, L.; Yan, F. High-Performance Ideal Bandgap Sn-Pb Mixed Perovskite Solar Cells Achieved by MXene Passivation. *Small* **2024**, *20* (47), 2403920.
- (59) Yu, X.; Sun, X.; Zhu, Z.; Li, Z. Stabilization Strategies of Buried Interface for Efficient SAM-Based Inverted Perovskite Solar Cells. *Angew. Chemie Int. Ed.* **2025**, *64* (4), No. e202419608.
- (60) Levine, I.; Al-Ashouri, A.; Musiienko, A.; Hempel, H.; Magomedov, A.; Drevilkaukaite, A.; Getautis, V.; Menzel, D.; Hinrichs, K.; Unold, T.; Albrecht, S.; Dittrich, T. Charge Transfer Rates and Electron Trapping at Buried Interfaces of Perovskite Solar Cells. *Joule* **2021**, *5* (11), 2915–2933.
- (61) Stoumpos, C. C.; Malliakas, C. D.; Kanatzidis, M. G. Semiconducting Tin and Lead Iodide Perovskites with Organic Cations: Phase Transitions, High Mobilities, and Near-Infrared Photoluminescent Properties. *Inorg. Chem.* **2013**, *52* (15), 9019–9038.
- (62) Jeon, N. J.; Noh, J. H.; Yang, W. S.; Kim, Y. C.; Ryu, S.; Seo, J.; Seok, S., II Compositional Engineering of Perovskite Materials for High-Performance Solar Cells. *Nature* **2015**, *517* (7535), 476–480.
- (63) Nie, W.; Tsai, H.; Asadpour, R.; Blancon, J.-C.; Neukirch, A. J.; Gupta, G.; Crochet, J. J.; Chhowalla, M.; Tretiak, S.; Alam, M. A.; Wang, H.-L.; Mohite, A. D. High-Efficiency Solution-Processed Perovskite Solar Cells with Millimeter-Scale Grains. *Science* **2015**, *347* (6221), 522–525.
- (64) Jeon, N. J.; Noh, J. H.; Kim, Y. C.; Yang, W. S.; Ryu, S.; Seok, S., II Solvent Engineering for High-Performance Inorganic-Organic Hybrid Perovskite Solar Cells. *Nat. Mater.* **2014**, *13* (9), 897–903.
- (65) Koch, N. Energy Levels at Interfaces between Metals and Conjugated Organic Molecules. *J. Phys.: Condens. Matter* **2008**, *20* (18), 184008.
- (66) Endres, J.; Egger, D. A.; Kulbak, M.; Kerner, R. A.; Zhao, L.; Silver, S. H.; Hodes, G.; Rand, B. P.; Cahen, D.; Kronik, L.; Kahn, A. Valence and Conduction Band Densities of States of Metal Halide Perovskites: A Combined Experimental-Theoretical Study. *J. Phys. Chem. Lett.* **2016**, *7* (14), 2722–2729.
- (67) Zu, F.; Amsalem, P.; Egger, D. A.; Wang, R.; Wolff, C. M.; Fang, H.; Loi, M. A.; Neher, D.; Kronik, L.; Duhm, S.; Koch, N. Constructing the Electronic Structure of CH₃NH₃PbI₃ and CH₃NH₃PbBr₃ Perovskite Thin Films from Single-Crystal Band Structure Measurements. *J. Phys. Chem. Lett.* **2019**, *10* (3), 601–609.
- (68) Tersoff, J. Theory of Semiconductor Heterojunctions: The Role of Quantum Dipoles. *Phys. Rev. B* **1984**, *30* (8), 4874–4877.
- (69) Akatsuka, A.; Truong, M. A.; Wakamiya, A.; Kapił, G.; Hayase, S.; Yoshida, H. A Universal Model for Energy Level Alignment at Interfaces of Hole-Collecting Monolayers in p-i-n Perovskite Solar Cells. *ChemRxiv* **2025**, 1.
- (70) Song, D.; Shin, S. W.; Wu, H.-P.; Diau, E. W.-G.; Correa-Baena, J.-P. Toward Maximizing Hole Selection with Self-Assembled Monolayers in Sn-Based Perovskite Solar Cells. *ACS Energy Lett.* **2025**, *10* (3), 1292–1312.
- (71) Xu, J.; Huang, S.; Wang, Z. First Principle Study on the Electronic Structure of Fluorine-Doped SnO₂. *Solid State Commun.* **2009**, *149* (13–14), 527–531.
- (72) Schultz, T.; Lenz, T.; Kotadiya, N.; Heimel, G.; Glasser, G.; Berger, R.; Blom, P. W. M.; Amsalem, P.; de Leeuw, D. M.; Koch, N. Reliable Work Function Determination of Multicomponent Surfaces and Interfaces: The Role of Electrostatic Potentials in Ultraviolet Photoelectron Spectroscopy. *Adv. Mater. Interfaces* **2017**, *4* (19), 1700324.
- (73) Schultz, T.; Amsalem, P.; Kotadiya, N. B.; Lenz, T.; Blom, P. W. M.; Koch, N. Importance of Substrate Work Function Homogeneity for Reliable Ionization Energy Determination by Photoelectron Spectroscopy. *Phys. status solidi* **2019**, *256* (2), 1800299.
- (74) Chen, X.; Kamat, P. V.; Janáky, C.; Samu, G. F. Charge Transfer Kinetics in Halide Perovskites: On the Constraints of Time-Resolved Spectroscopy Measurements. *ACS Energy Lett.* **2024**, *9* (6), 3187–3203.
- (75) Chen, X.; Pasanen, H. P.; Khan, R.; Tkachenko, N. V.; Janáky, C.; Samu, G. F. Effect of Single-Crystal TiO₂/Perovskite Band Alignment on the Kinetics of Electron Extraction. *J. Phys. Chem. Lett.* **2024**, *15* (7), 2057–2065.
- (76) Zhou, X.; Zhang, L.; Yu, J.; Wang, D.; Liu, C.; Chen, S.; Li, Y.; Li, Y.; Zhang, M.; Peng, Y.; Tian, Y.; Huang, J.; Wang, X.; Guo, X.; Xu, B. Integrated Ideal-Bandgap Perovskite/Bulk-Heterojunction Solar Cells with Efficiencies > 24%. *Adv. Mater.* **2022**, *34* (40), 2205809.
- (77) Zong, Y.; Wang, N.; Zhang, L.; Ju, M.; Zeng, X. C.; Sun, X. W.; Zhou, Y.; Pature, N. P. Homogenous Alloys of Formamidinium Lead Triiodide and Cesium Tin Triiodide for Efficient Ideal-Bandgap Perovskite Solar Cells. *Angew. Chemie Int. Ed.* **2017**, *56* (41), 12658–12662.
- (78) Zong, Y.; Zhou, Z.; Chen, M.; Pature, N. P.; Zhou, Y. Lewis-Adduct Mediated Grain-Boundary Functionalization for Efficient Ideal-Bandgap Perovskite Solar Cells with Superior Stability. *Adv. Energy Mater.* **2018**, *8* (27), 1800997.
- (79) Ke, W.; Spanopoulos, I.; Tu, Q.; Hadar, I.; Li, X.; Shekhawat, G. S.; Dravid, V. P.; Kanatzidis, M. G. Ethylenediammonium-Based “Hollow” Pb/Sn Perovskites with Ideal Band Gap Yield Solar Cells with Higher Efficiency and Stability. *J. Am. Chem. Soc.* **2019**, *141* (21), 8627–8637.

(80) Tong, J.; Gong, J.; Hu, M.; Yadavalli, S. K.; Dai, Z.; Zhang, F.; Xiao, C.; Hao, J.; Yang, M.; Anderson, M. A.; Ratcliff, E. L.; Berry, J. J.; Padture, N. P.; Zhou, Y.; Zhu, K. High-Performance Methylammonium-Free Ideal-Band-Gap Perovskite Solar Cells. *Matter* **2021**, *4* (4), 1365–1376.

(81) Yang, Z.; Rajagopal, A.; Jen, A. K. -Y. Ideal Bandgap Organic-Inorganic Hybrid Perovskite Solar Cells. *Adv. Mater.* **2017**, *29* (47), 1704418.

(82) Zhou, X.; Zhang, L.; Wang, X.; Liu, C.; Chen, S.; Zhang, M.; Li, X.; Yi, W.; Xu, B. Highly Efficient and Stable GABr-Modified Ideal-Bandgap (1.35 eV) Sn/Pb Perovskite Solar Cells Achieve 20.63% Efficiency with a Record Small Voc Deficit of 0.33 V. *Adv. Mater.* **2020**, *32* (14), 1908107.

(83) Chi, D.; Huang, S.; Zhang, M.; Mu, S.; Zhao, Y.; Chen, Y.; You, J. Composition and Interface Engineering for Efficient and Thermally Stable Pb-Sn Mixed Low-Bandgap Perovskite Solar Cells. *Adv. Funct. Mater.* **2018**, *28* (51), 1804603.

(84) Hu, M.; Chen, M.; Guo, P.; Zhou, H.; Deng, J.; Yao, Y.; Jiang, Y.; Gong, J.; Dai, Z.; Zhou, Y.; Qian, F.; Chong, X.; Feng, J.; Schaller, R. D.; Zhu, K.; Padture, N. P.; Zhou, Y. Sub-1.4eV Bandgap Inorganic Perovskite Solar Cells with Long-Term Stability. *Nat. Commun.* **2020**, *11* (1), 151.